

Article

# Ceramized Fabrics and Their Integration in a Semi-Pilot Plant for the Photodegradation of Water Pollutants

Lara Faccani, Simona Ortelli \* , Magda Blosi and Anna Luisa Costa 

Institute of Science and Technology for Ceramics—Italian National Research Council, Via Granarolo 64, I-48018 Faenza, RA, Italy; lara.faccani@istec.cnr.it (L.F.); magda.blosi@istec.cnr.it (M.B.); anna.costa@istec.cnr.it (A.L.C.)

\* Correspondence: simona.ortelli@istec.cnr.it; Tel.: +39-0546-69-9729

**Abstract:** The use of nano-photocatalysts for the water/wastewater purifications, particularly in developing regions, offers promising advantages over conventional technologies. TiO<sub>2</sub>-based photocatalysts deposited on fabrics represent an efficient solution for obtaining heterogeneous photocatalysts, which are easily adaptable in the already installed water treatment plants or air purification systems. Despite the huge effort spent to develop and characterize novel nano-photocatalysts, which are especially active under solar light, knowledge gaps still persist for their full-scale application, starting from the reactor design and scale-up and the evaluation of the photocatalytic efficiency in pre-pilot scenarios. In this study, we offered easily scalable solutions for adapting TiO<sub>2</sub>-based photocatalysts, which are deposited on different kinds of fabrics and implemented in a 6 L semi-pilot plant, using the photodegradation of Rhodamine B (RhB) as a model of water pollution. We took advantage of a multi-variable optimization approach to identify the best design options in terms of photodegradation efficiency and turnover frequency (TOF). Surprisingly, in the condition of use, the irradiation with a light-emitting diode (LED) visible lamp appeared as a valid alternative to the use of UV LED. The identification of the best design options in the semi-pilot plant allowed scaling up the technology in a 100 L pilot plant suitable for the treatment of industrial wastewater.

**Keywords:** photodegradation; nanoparticles; semi-pilot plant; fabric



**Citation:** Faccani, L.; Ortelli, S.; Blosi, M.; Costa, A.L. Ceramized Fabrics and Their Integration in a Semi-Pilot Plant for the Photodegradation of Water Pollutants. *Catalysts* **2021**, *11*, 1418. <https://doi.org/10.3390/catal11111418>

Academic Editors: Stéphanie Lambert and Julien Mahy

Received: 20 October 2021

Accepted: 19 November 2021

Published: 22 November 2021

**Publisher's Note:** MDPI stays neutral with regard to jurisdictional claims in published maps and institutional affiliations.



**Copyright:** © 2021 by the authors. Licensee MDPI, Basel, Switzerland. This article is an open access article distributed under the terms and conditions of the Creative Commons Attribution (CC BY) license (<https://creativecommons.org/licenses/by/4.0/>).

## 1. Introduction

Clean water is essential for life, and ensuring the availability and sustainable management of water and sanitation became in 2015 one of 17 goals world leaders agreed upon in order to achieve a better world in 2030 [1]. Organic compounds, toxic pesticides, and manure emissions from each industry are polluting drinking water and rivers, which is becoming a worldwide contamination with increased severity. The wide area of water pollution, diversification, and non-biodegradable problems has become a problem that cannot be solved by the natural cleansing cycle [2]. New technologies, as the nanotechnology, are developing to improve the current methods of remediation of water [3–6]. Metal oxide semiconductor nanoparticles (NPs), in particular TiO<sub>2</sub>, have attracted particular attention due to their photocatalytic properties [7]. The photocatalytic activity of TiO<sub>2</sub> is induced by UV light excitation with the consequent formation of electron<sup>-</sup>/hole<sup>+</sup> pairs. The released electrons can react with water and oxygen molecules on the surface to form free radicals [8]. These species are very reactive and able to degrade most of the organic compounds as well as biological contaminants to its mineral components, i.e., carbon dioxide and water [9].

The use of nano-photocatalysts for the water/wastewater purifications, particularly in developing regions, offers promising advantages over conventional technologies, such as low cost, simplicity, environmental friendliness, wide-ranging efficiency, and the capacity to break down traces of a wide variety of organic molecules, including viruses and chlorine-resistant organisms [10]. Despite the huge effort spent to develop and characterize novel nano-photocatalysts, which are especially active under solar light, knowledge gaps still

persist for their full-scale application, starting from the reactor design and scale-up and the evaluation of the photocatalytic efficiency in pre-pilot scenarios [11,12]. One of the main objectives addressed by more recent studies is to extend the use of TiO<sub>2</sub>-based photocatalysts to solar (visible) light for the application in areas without electricity or as a sustainable solution to avoid the use of bio-hazardous and costly UV light [13–16]. To respond to this very urgent and necessary need, different pollutant treatments with visible light-responsive photocatalysts have been developed, which are mainly based on TiO<sub>2</sub> modification [17]; nevertheless, the majority of works are carried out on a laboratory scale, and the introduction of other materials into TiO<sub>2</sub> dramatically increases the complexity of the photocatalyst preparation and cost, and the modification with heavy metals or harmful organics could even improve the degree of environment pollution [18,19].

Moreover, the scale-up of nano-TiO<sub>2</sub>-based photocatalytic technology in water depuration systems is strongly influenced by the need to immobilize the photocatalysts in large available, low weight, high mechanical flexibility supports, allowing an easy implementation in many different geometry water treatment reactors and the easy recovery and regeneration of photocatalysts. So, thanks to their affinity for TiO<sub>2</sub> NPs, hydrophilic fabrics are particularly suitable supports for hosting nanostructured coatings with high washing fastness [13,17].

In this work, we focused on the optimization of TiO<sub>2</sub>-based photocatalytic fabrics, which were implemented in a semi-pilot plant scale (6 L capacity) reactor, investigating the quantum efficiency of TiO<sub>2</sub>, when irradiated by both UV and visible light-emitting diode (LED) lights, using Rhodamine B (RhB) as a reaction model and identified the best design options, comparing catalyst and fabric properties, process parameters, and type of irradiation.

## 2. Results and Discussion

### 2.1. Characterization of TiO<sub>2</sub>-Based Nanosuspension

The hydrodynamic diameter, Z-potential, and p*H*<sub>i.e.p.</sub> values of pristine materials and TiO<sub>2</sub>-based nanosuspensions are reported in Table 1. A slight increase in the hydrodynamic diameter and zeta potential is observed in samples obtained after resin treatment (TACR and SiO<sub>2</sub>-R). This is due to a decrease in the colloidal stability coupled with the pH change. On the other hand, a significant increase in the hydrodynamic diameter in the TiO<sub>2</sub>:SiO<sub>2</sub> sample is caused by both the steric hindrance of SiO<sub>2</sub> heterocoagulated on the TiO<sub>2</sub> surface [20] and the consequent electrostatic destabilization due to the progressive neutralization of the TiO<sub>2</sub> surface charge with the increase in negatively charged SiO<sub>2</sub> content. This was further demonstrated by the shift of the p*H*<sub>i.e.p.</sub> toward acidic pH (Table 1). The TiO<sub>2</sub>:SiO<sub>2</sub> sample was obtained by the self-assembled heterocoagulation process between TAC and SiO<sub>2</sub>-R, which exhibit, at the working pH = 4, potentials opposite in sign and high enough to preserve colloidal stabilization (Figure 1). Therefore, TAC and SiO<sub>2</sub>-R were able to promote the heterocoagulation between positive TiO<sub>2</sub> and negative SiO<sub>2</sub> nanosurfaces.

**Table 1.** Hydrodynamic diameter (nm), Z-potential (mV), and p*H*<sub>i.e.p.</sub> of pristine materials and TiO<sub>2</sub>-based nanosuspension.

Sample	d <sub>DLS</sub> (nm)	Z Potential (mV)	pH	p <i>H</i> <sub>i.e.p.</sub>
TAC	27	+36	1.5	7.7
TACR	29	+45	4	5.2
SiO <sub>2</sub>	30	−45	7	<1.5
SiO <sub>2</sub> -R	37	−34	4	<1.5
TiO <sub>2</sub> :SiO <sub>2</sub>	317	+38	4	5.2

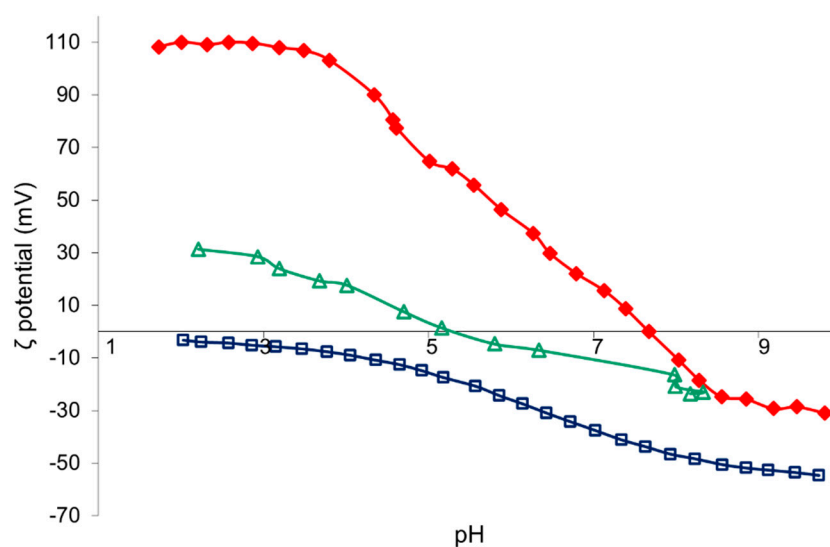


**Figure 1.** Z-potential vs. pH curves of TAC (red), SiO<sub>2</sub> (blue), and TiO<sub>2</sub>:SiO<sub>2</sub> (green) nanosuspension.

## 2.2. Characterization of Fabrics

A basic morphological characterization of fabrics, used as support for obtaining nano-TiO<sub>2</sub>-coated photocatalysts, was carried out by optical microscope (Figure 2).

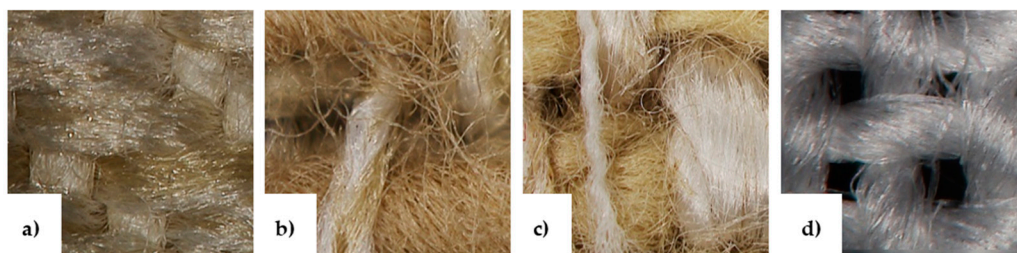


**Figure 2.** Optical microscopy images of untreated fabrics: (a) SP; (b) SC; (c) SM; (d) C.

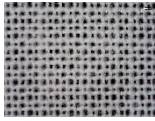
The images (Figure 2) show the differences of color, warp, and weft of the target fabrics. SP, SC, and SM fabrics are characterized by very intertwined fibers, whilst the weave of the C fabric is more regular and expanded than other fabrics. This can explain the significant differences in the absorption of the TiO<sub>2</sub>-based nanosuspensions (TACR and TiO<sub>2</sub>:SiO<sub>2</sub>), as demonstrated by the add-on percentage (AO%) reported in Table 2. In fact, the fabric C being characterized by a large weave and low weight (Table 3) adsorbs half the amount adsorbed by the other fabrics.

**Table 2.** AO% parameters calculated.

Fabric	AO% (TACR)	AO% (TiO <sub>2</sub> :SiO <sub>2</sub> )
SP	5.9	8
SC	8.4	n.a.
SM	6.2	n.a.
C	3.8	3

n.a. not available.

**Table 3.** Fabrics used as supports for nano-TiO<sub>2</sub>-based coatings.

Code	Images	Composition	g/m <sup>2</sup>
SP		65% cotton 35% polyester	450
SC		65% cotton 35% polyester	500
SM		Not available	640
C		100% cotton	100

In order to evaluate the hydrophilicity of fabrics and estimate the adsorption capacity of the textile supports, before and after the TiO<sub>2</sub> treatment (TACR), contact angle measurements were performed. The results are reported in Table 4.

**Table 4.** Contact angle measurements on untreated and TACR coated fabrics.

Fabric	Untreated	Coated
SP	121 ± 1	121 ± 3
SC	113 ± 1	n.d.
SM	n.d.	n.d.
C	n.d.	122 ± 4

n.d. not determined.

In general, all samples show hydrophilic properties, and no significant differences between untreated and treated fabrics are found. Specifically, the SM fabric exhibits very high hydrophilic behavior both on untreated and treated samples. In fact, the water drop is absorbed so quickly that during the contact angle measurements, the values are not detectable. This also occurs for untreated C and treated SC fabrics. In the case of SC fabric, an increase in hydrophilicity induced by TiO<sub>2</sub> treatment is found. Otherwise, a decrease in hydrophilicity induced by TiO<sub>2</sub> treatment was found in the C sample fabric. In any case, no clear correlation between the variation of hydrophilicity between different samples and the photocatalytic efficiency was found, as the results discussed in the following paragraphs show.

### 2.3. Optimization of Photocatalytic Process

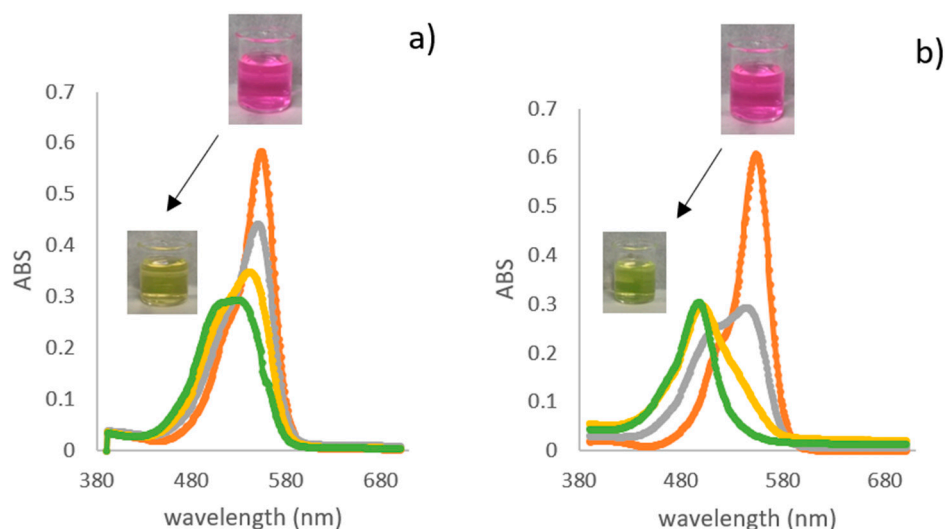
#### 2.3.1. Effect of TiO<sub>2</sub>-Based Coatings Composition

Using SP as the target fabric, we evaluated the photocatalytic efficiency of TACR and TiO<sub>2</sub>:SiO<sub>2</sub>-based coatings under both UV and visible light irradiation. Very low differences were observed between TiO<sub>2</sub> and TiO<sub>2</sub>:SiO<sub>2</sub> compositions (Table 5). This result confirms the different mechanism occurring when the photodegradation of TiO<sub>2</sub> is tested at a liquid and gas state. In fact, in a previous study [21], using NO<sub>x</sub> abatement (DeNO<sub>x</sub>) as the experimental model, we found that the presence of SiO<sub>2</sub> significantly improved the efficiency of the photocatalyst.

**Table 5.** Comparison between different TiO<sub>2</sub>-based photocatalysts. Tests carried out with SP fabrics under UV and visible light.

Irradiation Light	Coating	Photocatalytic Efficiency %
Visible	TACR	49
	TiO <sub>2</sub> :SiO <sub>2</sub>	51
UV	TACR	64
	TiO <sub>2</sub> :SiO <sub>2</sub>	60

The RhB photodegradation of the two photocatalysts over time is represented in Figure 3, showing a progressive decrease in the absorbance of the RhB peak at 554 nm. Moreover, for both photocatalysts, a blue-shift of the  $\lambda_{\max}$  was detected. This is associated to a de-ethylation of RhB molecules, which is in agreement with the hypothesized RhB degradation mechanism, in the presence of supported photocatalysts. The assessment of photocatalytic efficiency was done by considering the maximum of the absorbance peaks, allowing an estimation of the overall reactivity, because we referred to the capacity of the catalyst to photodegrade the dye and its by-products. The higher shift detected in the case of the TiO<sub>2</sub>:SiO<sub>2</sub> photocatalyst can be attributed to a complete conversion of the N,N,N',N'-tetraethylated rhodamine molecule ( $\lambda_{\max}$  554 nm) to de-ethylated rhodamine ( $\lambda_{\max}$  498 nm), as a consequence of the attack of oxidative radicals against N-ethyl group [22], which was not achieved in the case of TACR. This was further confirmed by Chen et al. [23] that showed different absorption mechanisms and consequently different degradation mechanisms using TiO<sub>2</sub> or the TiO<sub>2</sub>:SiO<sub>2</sub> composite. In fact, they declare that in the case of RhB absorption on TiO<sub>2</sub>:SiO<sub>2</sub>, the chromophore is absorbed by the photocatalyst through the diethylamino groups while in the case of TiO<sub>2</sub>, it is absorbed through the carboxyl groups. This difference results in an attack of the chromophore ring and its cleavage in the RhB-TiO<sub>2</sub> case, while in the RhB-TiO<sub>2</sub>:SiO<sub>2</sub> case, the auxochromic groups are attacked and produce the de-ethylation of the alkylamine group. Moreover, they found that the blue-shift phenomenon due to the RhB de-ethylation is more evident under visible light than UV, which is because the UV radiation directly excites the TiO<sub>2</sub>, while under visible light, it is the RhB absorbed on the surface of the photocatalyst to subsequently produce the active oxygen species.

**Figure 3.** Absorbance of RhB solutions after irradiation under visible light at 0 min (orange), 40 min (gray), 80 min (yellow), and 100 min (green). Time 0:  $\lambda_{\max}$  554 nm; time 100:  $\lambda_{\max}$  527 nm for TACR (a) and 498 nm for TiO<sub>2</sub>:SiO<sub>2</sub> (b).

### 2.3.2. Effect of Temperature

The dependence of photocatalytic performance on temperature has been widely investigated in the literature, and it is still under debate, with increasing temperature promoting phenomena such as the desorption of adsorbed reactants and the rate of recombination of photogenerated electron/hole pairs that are detrimental for the photocatalysis [24,25]. Otherwise, it is well known that the temperature influences the reaction kinetics, enhancing the activation energy and so speeding the photodegradation process [26,27]. Photodegradation tests using SP fabrics coated with TiO<sub>2</sub>:SiO<sub>2</sub>, under both UV and visible light sources, were compared at three working temperatures: 15 °C, 25 °C (room temperature), and 38 °C. The results are shown in Table 6. Under UV LED irradiation, the photocatalytic activity decreases by increasing the temperature, whilst in the case of visible LED, no significant trend was observed. The dependence of photodegradation efficiency by temperature is the result of synergetic (increase in activation energy, increase in charge transfer kinetic) and detrimental effects (the recombination of charge carriers and the altered adsorption equilibrium of reactants such as dye molecules, water, and oxygen) [24,26–28]. Therefore, in this case, the best compromise is working at room temperature, matching environmental and economic requirements [29].

**Table 6.** Effect of temperature. Tests carried out with TiO<sub>2</sub>:SiO<sub>2</sub>-coated SP samples, under both UV and visible LEDs.

Irradiation	Temperature °C	Photocatalytic Efficiency %
Visible	15	55
	25	51
	38	57
UV	15	63
	25	60
	38	59

### 2.3.3. Effect of Fabric Substrate

In order to investigate the effect of fabric substrates vs. type of irradiation (UV and visible light sources), we carried out photocatalytic tests with TACR-coated fabrics, and the results are reported in Table 7.

**Table 7.** Effect of fabric substrates. Tests carried out with TACR at T° = 25 °C, under both UV and visible light sources.

Fabric	Photocatalytic Efficiency %	
	UV LED	Visible LED
SP	49	64
SC	64	54
SM	65	61
C	67	57

Overall samples showed a comparable photodegradation efficiency despite the type of fabrics used and the type of irradiation source. Nevertheless, the fabric composition and structure seem to affect the efficiency; the SP sample is even more reactive under a visible source. The reactivity shown by the samples irradiated by visible LED was surprising, considering that the TACR crystalline phase, corresponding to anatase with 16% of brookite [30], has a band-gap, previously measured of 3.26 eV, that restricts its use only to the ultra-violet range of light. Considering the UV light fraction intensity measured on the fabric surface—UV LED (48.5 W/m<sup>2</sup>) and visible LED (4.3 × 10<sup>−3</sup> W/m<sup>2</sup>), it is evident that in the case of a visible lamp, the few photons achieving the fabric surface have enough energy to activate the catalyst, and they are responsible for the photodegradation reactivity, which is comparable with that obtained irradiating the samples with UV LED,

with a UV irradiation intensity that is five orders of magnitude higher. This result is quite unexpected because even if it is reported that a few photons of energy (i.e., as low as  $1 \times 10^{-2} \text{ W/m}^2$ ) can induce the photo-generation of electron–hole pairs [31], high intensities ( $400\text{--}1000 \text{ W/m}^2$ ) are needed to achieve a high photocatalytic reaction rate, particularly in water disinfection treatment [32]. The really low intensity of ultraviolet radiation (UVR) needed to activate our photocatalysts encourages their use and activation under solar irradiation; considering that the UV light portion of the yearly average solar irradiance at sea level, on a clear day, is about a few units  $\text{W/m}^2$ , we can reasonably estimate that the UVR intensity of the sun is in large excess of the amount needed to activate our photocatalysts. From this perspective, the proposed  $\text{TiO}_2$ -based photocatalysts do not require costly and time-consuming doping treatments to be activated under visible LED or solar light, with consequent benefits from safety, environmental, and economic points of view [31].

In order to better compare the photocatalytic ability of coated fabrics and select the most suitable fabric support, we calculated the TOF parameter (Table 8). The results show that the C fabric presents the highest photoactivity, both under UV and visible LEDs. Considering the natural source of cotton (100% biodegradable), its high availability at low cost and the shown photo-induced reactivity under visible LED, which is one order of magnitude higher than the other photocatalyst, also irradiated by UV light, it is evident that the cotton photocatalyst under visible LED becomes the best choice, matching the criteria of sustainability and safety.

**Table 8.** TOF parameter calculated at time 100 min. Tests carried out with TACR at  $T^\circ = 25^\circ \text{C}$ , under both UV and visible light sources.

Fabric	Photocatalytic Efficiency %	
	UV LED	Visible LED
SP	$7.5 \times 10^{-5}$	$9.8 \times 10^{-5}$
SC	$8.9 \times 10^{-5}$	$7.5 \times 10^{-5}$
SM	$8.6 \times 10^{-5}$	$8.8 \times 10^{-5}$
C	$1.02 \times 10^{-3}$	$8.7 \times 10^{-4}$

#### 2.4. Process Scalability

The treated fabrics were integrated and tested in the LED-based semi-pilot photocatalytic reactor of Figure 4a. Figure 4b shows the pilot reactor based upon the best design options identified performing tests with the semi-pilot reactor. The performances obtained with the pilot plant and the evaluation about the scalability of the semi-pilot plant are the objective of a future study.

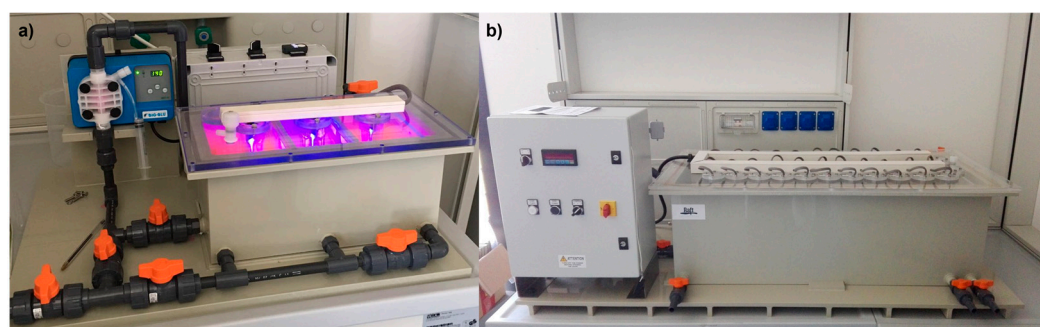


**Figure 4.** (a) LED-based semi-pilot photocatalytic reactor tested (6 L), used in this study; (b) Up-scaled reactor (100 L) built upon the best design options in the present study.

### 3. Materials and Methods

#### 3.1. Materials

TiO<sub>2</sub> nanosol (NAMA41, 6 wt %), called TAC and SiO<sub>2</sub> nanosol 40 wt % (Ludox<sup>®</sup> HS-40) were purchased from Colorobbia (Sovigliana, Vinci (FI), Italy) and Grace Davison (USA), respectively. Rhodamine B (dye content ≈ 95%) target dye, ion exchanger Dowex<sup>®</sup> 1 X 8 basic anion exchanger resin and ion exchanger Dowex<sup>®</sup> 50 W X 4 acidic cation exchanger resin were purchased from Sigma Aldrich (Milano, Italy).

#### 3.2. TiO<sub>2</sub>-Based Nanosuspensions

Acid TiO<sub>2</sub> nanosol (TAC, pH 1.5) was used to prepare two TiO<sub>2</sub>-based nanosuspensions: TACR and TiO<sub>2</sub>:SiO<sub>2</sub> suspensions. TACR was obtained diluting TAC at the 3 wt % concentration with distilled water (DI) water and treated with ion exchanger Dowex<sup>®</sup> 1 X 8 basic anion exchanger resin in order to increase the pH from 1.5 to 4. This increase in pH is necessary in order to avoid fabric damage caused by acidity, and the residual by the synthesis of original TiO<sub>2</sub> can reduce the photocatalytic activity [30]. TiO<sub>2</sub>:SiO<sub>2</sub> 3 wt % was prepared by the heterocoagulation method. SiO<sub>2</sub> nanosol 40 wt % (Ludox<sup>®</sup> HS-40) was diluted at the concentration 3 wt % with DI water and treated with ion exchange Dowex<sup>®</sup> 50 W X 4 acidic cationic exchanger resin in order to decrease the pH from 10 to 4 (SiO<sub>2</sub>-R). TiO<sub>2</sub> suspension (TACR) was dropped into SiO<sub>2</sub>-R suspension. The TiO<sub>2</sub>:SiO<sub>2</sub> sample was obtained through an electrostatic interaction between negatively charged silica nanoparticles and positively charged titania nanoparticles. The electrostatic interactions between SiO<sub>2</sub> and TiO<sub>2</sub> surfaces are promoted by mixing the sols in well-defined ratios and by ball milling for 24 h with zirconia spheres (diameter 5 mm) as grinding media.

#### 3.3. Ceramized Fabric

The coated fabrics was obtained via the dip-pad-curing method. The fabric was washed in an ultrasonic bath for 15 min in DI water and dried in an oven at 100 °C. Then, the washed fabric was dipped in a TiO<sub>2</sub>-based suspension for 5 min, squeezed in two rolls to eliminate the excess of suspension (pad stage), dried in a stove at 100 °C, and finally cured at 130 °C for 10 min in order to well fix the NPs to the fabric. A single impregnation was carried out achieving the final dry add-on value (AO%), which is defined as the percent amount of the finishing agent added to the fabric with respect to the initial weight of the latter, i.e.,

$$AO\% = \frac{W_f - W_i}{W_i} \times 100 \quad (1)$$

where  $w_i$  and  $w_f$  are the weights of the fabric before and after the dip-pad-curing process.

We tested four fabrics different in color, weight, and structure described in Table 3.

#### 3.4. Semi-Pilot Plant and Irradiation Source

The photocatalytic tests were carried out in a 6 L semi-pilot plant [33], as schematized in Figure 5. The semi-pilot plant was designed and built by RAFT s.r.l., (Montelupo Fiorentino (FI) Italy). It hosts two plastic windows for supporting ceramized fabrics (14.8 × 11.4 cm; 100 cm<sup>2</sup> fabric exposed area for each support), and on the top, there are three holes for UV or visible light lamps. The homogeneity of water flow was ensured through a peristaltic pump, and the feed bath was thermostated by a chiller (Julabo, F12). The LED strip lights were provided by the Wiva Group (Firenze, Italy). The visible LED light is characterized by a wide emission spectrum (Figure 6a) with a main peak at wavelength = 452 nm and a second peak at wavelength = 569 nm. The UV LED light has a very narrow emission spectrum with  $\lambda_{max} = 384$  nm (Figure 6b). The irradiance was calculated placing a radiometric UV probe (UV-A 315–400 nm) on the fabric surface in order to evaluate the UV component irradiance of the two light-emitting sources that resulted in  $4.3 \times 10^{-3}$  W/m<sup>2</sup> for visible light and 150 W/m<sup>2</sup> for UV light.

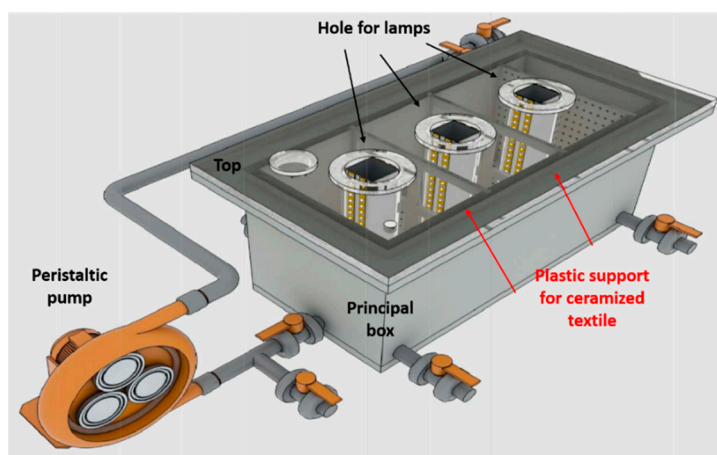


Figure 5. Schematized representation of a 6 L semi-pilot plant.

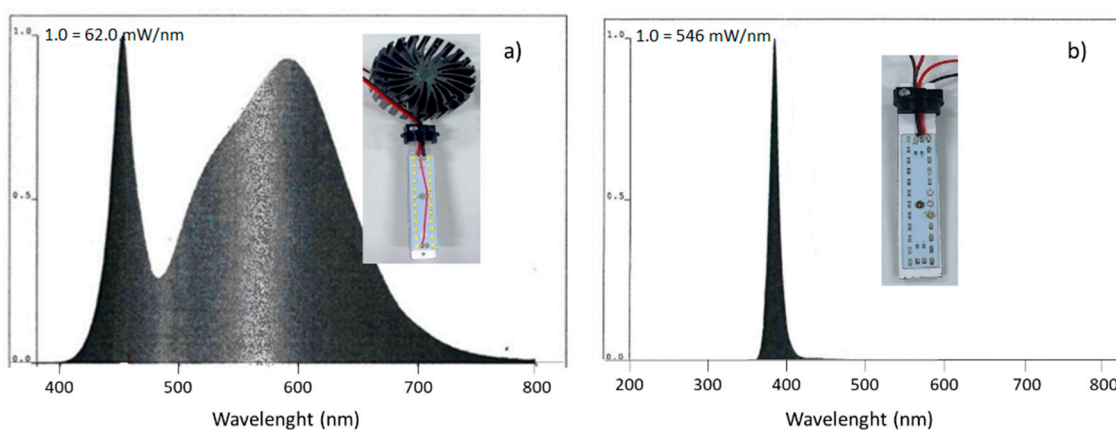


Figure 6. Emission spectrum of (a) visible LED light and (b) UV LED light, including photographs of the corresponding LED strips, mounting an air-cooling fan.

### 3.5. Characterization

#### 3.5.1. Dynamic Light Scattering/Electrophoretic Light Scattering

The hydrodynamic diameters and zeta potential distribution of TiO<sub>2</sub>-based suspensions, dispersed at 0.3 wt % in DI water, were evaluated by using a Zetasizer instrument (Malvern Instruments, Zetasizer Nano-ZS, Malvern, UK) based on the dynamic light scattering (DLS) and electrophoretic light scattering (ELS) techniques. For particle size distribution evaluation, about 1 mL of the sample was measured consecutively three times at 25 °C. The size distribution (nm) is reported as the intensity-weighted mean diameter derived from the cumulant analysis (Z-average) and is the average of three independent measurements. The reliability of the measurements was controlled by using the automatic attenuator (kept between 6 and 8) and the intercept autocorrelation function (<0.9) as quality criteria [4].

The zeta potential was measured on 700 µL of the sample at 25 °C, setting the measurement time, the attenuator position, and the applied voltage to automatic. After a 2 min temperature equilibration step, the samples were measured three times, and the data were obtained by averaging the three measurements. The data of zeta potential (mV) are derived by electrophoretic mobility using Smoluchowski's formula. The reliability of the measurements was controlled by check the phase plot graph.

The same instrument coupled with an automating titrating system was used to create zeta potential vs. pH curve to identify the pH at which the zeta potential sets to zero,

namely the isoelectric point ( $pH_{i.e.p.}$ ). The titrants used were 0.1M KOH solution and 0.1M HCl solution.

### 3.5.2. Characterization on Fabrics

The untreated fabrics were morphologically observed by optical microscope using a Hirox 3D digital microscope, RH200 with a magnitude of lens X35 and X50. Specifically, we observed the fabric weave, thickness, and color of a single fiber.

The hydrophilicity of untreated and TACR-treated fabrics was evaluated by contact angle analyses. The measurements were carried out using a KRUSS DSA 30 S instrument, the sessile drop as the drop deposition method at room temperature (25 °C), 20  $\mu$ L drop volume, and a tangent-fitting method.

### 3.6. Rhodamine B Degradation Tests

The photodegradation tests were carried out using Rhodamine B (RhB) as a model of organic trace pollutant. RhB is a synthetic dye that is commonly used in water remediation due to the easy detection of small concentrations by UV-Vis absorption analysis using a single beam spectrophotometer Hach Lange, DR3900. RhB imparts a deep magenta hue to its water solutions and displays a well-defined absorbance peak at 554 nm. In our experiment, we used 3.5 mg/L RhB concentration. The lamp was switched on outside the plant 30 min before starting the test in order to stabilize the power of emission; simultaneously, the ceramized textile was put into RhB solution to reach the adsorption–desorption equilibrium. In order to evaluate the degradation kinetics, an aliquot of 3 mL was withdrawn and analyzed every 20 min ( $A_x$ ) through UV-Vis analysis in the range of 350–700 nm to a final reaction time of 100 min. The  $A_x$  was measured in correspondence to the maximum of the absorbance peak detected, taking into account the shift of the initial absorbance peak of RhB. Before starting the degradation tests, after 30 min of absorption, the initial absorbance ( $A_0$ ) was determined. The order of photocatalytic degradation reactions was ascertained from the pseudo first-order kinetic model:

$$\ln\left(\frac{A_0}{A_x}\right) = k * t. \quad (2)$$

The photocatalytic efficiency was calculated at  $t = 100$  min. It indicates the ratio between the amount of reagent consumed and the amount of reagent initially present in the reaction environment, and it was determined by the following formula:

$$\text{Photocatalytic efficiency (\%)} = \left(1 - \frac{A_x}{A_0}\right) * 100 \quad (3)$$

where  $A_x$  is the peak value at time  $t$  and  $A_0$  is the peak value at time 0. In order to facilitate the comparison between the different photocatalysts, normalizing for the amount of catalyst and the time of exposure, the turnover frequency (TOF) parameter was calculated. The TOF parameter was calculated by following equation:

$$\text{TOF} = \frac{\left(\frac{\text{mol of product}}{t \text{ (s)}}\right)}{\text{mol of catalyst}} \quad (4)$$

where

mol of product is calculated as the initial concentration of reagent per efficiency reached at the time  $s$

mol of catalyst are the moles of the catalyst deposited on the exposure area of fabric calculated by the AO% parameter.

#### 4. Conclusions

In response to the still persisting knowledge gaps for the full-scale application of nano-photocatalysts in water/wastewater purification systems, we immobilized TiO<sub>2</sub>-based nanoparticles as the coating of fabrics, obtaining large available, low cost, highly flexible photocatalysts that allow an easy implementation in many different geometry water treatment reactors and the easy recovery and regeneration of photocatalysts. We implemented the obtained photocatalytic fabrics in a 6 L capacity semi-pilot plant and evaluated the degradation of RhB dye, which was used as a probe molecule, simulating the water pollution. We adopted a multi-variables optimization approach to look for the photoreactor operating parameters that mostly affected the photocatalytic performance and identified the best design option also in response to safety and sustainable criteria. We found that the 100% biodegradable cotton fabric irradiated by visible LED is the best candidate, because it showed a TOF higher than all the other samples, which was irradiated by both UV and visible light sources. The really low intensity of UV radiation-activating fabrics under visible LED expands the applicability of the technology to solar light, since the measured intensity of the UV radiation component, in visible LED, is much lower than the solar yearly average one. The findings from the multi-variable optimization study were translated into updated recommendations for the design and the technical application of these efficient and low-cost TiO<sub>2</sub>-based photocatalysts, which are suitable for developing a range of technologies aimed at environmental protection. The good results obtained encouraged the scale-up of the 6 L semi-pilot plant up to the 100 L pilot plant that has been built, even if the evaluation of photocatalytic performances is still under investigation.

**Author Contributions:** A.L.C., S.O., M.B. and L.F. conceived and designed the experiments; L.F. performed the experiments and analyzed the data; L.F., S.O. and A.L.C. wrote the paper. All authors have read and agreed to the published version of the manuscript.

**Funding:** This work was supported by the “ASINA” (Anticipating Safety Issues at the Design Stage of NANO Product Development) European project (H2020—GA 862444).

**Acknowledgments:** The authors acknowledge RAFT s.r.l. (Montelupo Fiorentino (FI), Italy) and Wiva Group SpA, (Firenze, Italy) for the support provided to the design and production of the (semi) pilot and pilot plants and the LED-lamps, respectively, used in this work.

**Conflicts of Interest:** The authors declare no conflict of interest.

#### References

1. Organizzazione delle Nazioni Unite. Trasformare il Nostro Mondo: L'Agenda 2030 per lo Sviluppo Sostenibile (Agenda2030). In *Risoluzione Adottata Dall'assemblea Gen. 25 Settembre 2015*; 2015. Available online: <https://unric.org/it/wp-content/uploads/sites/3/2019/11/Agenda-2030-Onu-italia.pdf> (accessed on 1 November 2021).
2. Lee, S.Y.; Park, S.J. TiO<sub>2</sub> photocatalyst for water treatment applications. *J. Ind. Eng. Chem.* **2013**, *19*, 1761–1769. [[CrossRef](#)]
3. Qu, X.; Alvarez, P.J.J.; Li, Q. Applications of nanotechnology in water and wastewater treatment. *Water Res.* **2013**, *47*, 3931–3946. [[CrossRef](#)]
4. Varenne, F.; Hillaireau, H.; Bataille, J.; Smadja, C.; Barratt, G.; Vauthier, C. Application of validated protocols to characterize size and zeta potential of dispersed materials using light scattering methods. *Colloids Surf. A Physicochem. Eng. Asp.* **2019**, *560*, 418–425. [[CrossRef](#)]
5. Gehrke, I.; Geiser, A.; Somborn-Schulz, A. Innovations in nanotechnology for water treatment. *Nanotechnol. Sci. Appl.* **2015**, *8*, 1–17. [[CrossRef](#)]
6. Qu, X.; Brame, J.; Li, Q.; Alvarez, P.J.J. Nanotechnology for a safe and sustainable water supply: Enabling integrated water treatment and reuse. *Acc. Chem. Res.* **2013**, *46*, 834–843. [[CrossRef](#)]
7. Liu, H.; Ma, H.T.; Li, X.Z.; Li, W.Z.; Wu, M.; Bao, X.H. The enhancement of TiO<sub>2</sub> photocatalytic activity by hydrogen thermal treatment. *Chemosphere* **2003**, *50*, 39–46. [[CrossRef](#)]
8. Yuranova, T.; Laub, D.; Kiwi, J. Synthesis, activity and characterization of textiles showing self-cleaning activity under daylight irradiation. *Catal. Today* **2007**, *122*, 109–117. [[CrossRef](#)]
9. Bellardita, M.; Di Paola, A.; Palmisano, L.; Parrino, F.; Buscarino, G.; Amadelli, R. Preparation and photoactivity of samarium loaded anatase, brookite and rutile catalysts. *Appl. Catal. B Environ.* **2011**, *104*, 291–299. [[CrossRef](#)]
10. Adly, M.S.; El-Dafrawy, S.M.; El-Hakam, S.A. Application of nanostructured graphene oxide/titanium dioxide composites for photocatalytic degradation of rhodamine B and acid green 25 dyes. *J. Mater. Res. Technol.* **2019**, *8*, 5610–5622. [[CrossRef](#)]

11. Khodadadian, F.; de Boer, M.W.; Poursaeidesfahani, A.; van Ommen, J.R.; Stankiewicz, A.I.; Lakerveld, R. Design, characterization and model validation of a LED-based photocatalytic reactor for gas phase applications. *Chem. Eng. J.* **2018**, *333*, 456–466. [[CrossRef](#)]
12. Li, R.; Li, T.; Zhou, Q. Impact of titanium dioxide (TiO<sub>2</sub>) modification on its application to pollution treatment—A review. *Catalysts* **2020**, *10*, 804. [[CrossRef](#)]
13. Costa, A.L.; Ortelli, S.; Blosi, M.; Albonetti, S.; Vaccari, A.; Dondi, M. TiO<sub>2</sub> based photocatalytic coatings: From nanostructure to functional properties. *Chem. Eng. J.* **2013**, *225*, 880–886. [[CrossRef](#)]
14. Mahanta, U.; Khandelwal, M.; Suresh Deshpande, A. TiO<sub>2</sub>@SiO<sub>2</sub> nanoparticles for methylene blue removal and photocatalytic degradation under natural sunlight and low-power UV light. *Appl. Surf. Sci.* **2021**, *576*, 151745. [[CrossRef](#)]
15. Basavarajappa, P.S.; Patil, S.B.; Ganganagappa, N.; Reddy, K.R.; Raghu, A.V.; Reddy, C.V. Recent progress in metal-doped TiO<sub>2</sub>, non-metal doped/codoped TiO<sub>2</sub> and TiO<sub>2</sub> nanostructured hybrids for enhanced photocatalysis. *Int. J. Hydrogen Energy* **2020**, *45*, 7764–7778. [[CrossRef](#)]
16. Dong, X.; Xu, J.; Kong, C.; Zeng, X.; Wang, J.; Zhao, Y.; Zhang, W. Synthesis of β-FeOOH/TiO<sub>2</sub>/SiO<sub>2</sub> by melting phase separation-hydrothermal method to improve photocatalytic performance. *Ceram. Int.* **2021**, *47*, 32303–32309. [[CrossRef](#)]
17. Ortelli, S.; Malucelli, G.; Blosi, M.; Zanoni, I.; Costa, A.L. NanoTiO<sub>2</sub> @DNA complex: A novel eco, durable, fire retardant design strategy for cotton textiles. *J. Colloid Interface Sci.* **2019**, *546*, 174–183. [[CrossRef](#)] [[PubMed](#)]
18. Factories, H.; Study, A.C.; Plant, P.; Joseane, J.; Mesa, M.; Sebasti, J.; Gonz, W.; Rojas, H.; Murcia Mesa, J.J.; Hernández Niño, J.S.; et al. Photocatalytic Treatment of Stained Wastewater Coming from Handicraft Factories. A Case Study at the Pilot Plant Level. *Water* **2021**, *13*, 2705.
19. Sciscenko, I.; Mestre, S.; Climent, J.; Valero, F.; Escudero-Oñate, C.; Oller, I.; Arques, A. Magnetic photocatalyst for wastewater tertiary treatment at pilot plant scale: Disinfection and enrofloxacin abatement. *Water* **2021**, *13*, 329. [[CrossRef](#)]
20. Qian, W.; Zhaoqun, W.; Xuanfeng, K.; Xiaodan, G.; Gi, X. A facile strategy for controlling the self-assembly of nanocomposite particles based on colloidal steric stabilization theory. *Langmuir* **2008**, *24*, 7778–7784. [[CrossRef](#)]
21. Ortelli, S.; Poland, C.A.; Baldi, G.; Costa, A.L. Silica matrix encapsulation as a strategy to control ROS production while preserving photoreactivity in nano-TiO<sub>2</sub>. *Environ. Sci. Nano* **2016**, *3*, 602–610. [[CrossRef](#)]
22. Ortelli, S.; Blosi, M.; Albonetti, S.; Vaccari, A.; Dondi, M.; Costa, A.L. TiO<sub>2</sub> based nano-photocatalysis immobilized on cellulose substrates. *J. Photochem. Photobiol. A Chem.* **2014**, *276*, 58–64. [[CrossRef](#)]
23. Chen, F.; Zhao, J.; Hidaka, H. Highly selective deethylation of Rhodamine B: Adsorption and photooxidation pathways of the dye on the TiO<sub>2</sub>/SiO<sub>2</sub> composite photocatalyst. *Int. J. Photoenergy* **2003**, *5*, 209–217. [[CrossRef](#)]
24. Meng, Y.; Xia, S.; Pan, G.; Xue, J.; Jiang, J.; Ni, Z. Preparation and photocatalytic activity of composite metal oxides derived from Salen-Cu(II) intercalated layered double hydroxides. *Korean J. Chem. Eng.* **2017**, *34*, 2331–2341. [[CrossRef](#)]
25. Meng, F.; Liu, Y.; Wang, J.; Tan, X.; Sun, H.; Liu, S.; Wang, S. Temperature dependent photocatalysis of g-C<sub>3</sub>N<sub>4</sub>, TiO<sub>2</sub> and ZnO: Differences in photoactive mechanism. *J. Colloid Interface Sci.* **2018**, *532*, 321–330. [[CrossRef](#)]
26. Barakat, N.A.M.; Kanjwal, M.A.; Chronakis, I.S.; Kim, H.Y. Influence of temperature on the photodegradation process using Ag-doped TiO<sub>2</sub> nanostructures: Negative impact with the nanofibers. *J. Mol. Catal. A Chem.* **2013**, *366*, 333–340. [[CrossRef](#)]
27. Chen, Y.W.; Hsu, Y.H. Effects of reaction temperature on the photocatalytic activity of TiO<sub>2</sub> with Pd and Cu cocatalysts. *Catalysts* **2021**, *11*, 966. [[CrossRef](#)]
28. Liu, B.; Zhao, X.; Parkin, I.P.; Nakata, K. *Charge Carrier Transfer in Photocatalysis*; Elsevier: Amsterdam, The Netherlands, 2020; Volume 31, ISBN 9780081028902.
29. Alisawi, H.A.O. Performance of wastewater treatment during variable temperature. *Appl. Water Sci.* **2020**, *10*, 89. [[CrossRef](#)]
30. Ortelli, S.; Costa, A.L.; Dondi, M. TiO<sub>2</sub> nanosols applied directly on textiles using different purification treatments. *Materials* **2015**, *8*, 7988–7996. [[CrossRef](#)]
31. Chong, M.N.; Jin, B.; Chow, C.W.K.; Saint, C. Recent developments in photocatalytic water treatment technology: A review. *Water Res.* **2010**, *44*, 2997–3027. [[CrossRef](#)]
32. Rincón, A.G.; Pulgarin, C. Photocatalytical inactivation of E. coli: Effect of (continuous-intermittent) light intensity and of (suspended-fixed) TiO<sub>2</sub> concentration. *Appl. Catal. B Environ.* **2003**, *44*, 263–284. [[CrossRef](#)]
33. Ortelli, S.; Costa, A.L.; Torri, C.; Samori, C.; Galletti, P.; Vainas, C.; Varesano, A.; Bonura, L.; Bianchi, G. Innovative and sustainable production of Biopolymers. In *Factories of the Future: The Italian Flagship Initiative*; Tolio, T., Copani, G., Terkaj, W., Eds.; Springer International Publishing: Cham, Switzerland, 2019; Chapter 6, ISBN 9783319943589.